



**HAL**  
open science

## Optimization and design of a diffuse optical wireless sensor network

Thomas Kamalakis, Zabih Ghassemlooy, Stanislav Zvanovec, Luis Nero Alves, Mohammad Khalighi

► **To cite this version:**

Thomas Kamalakis, Zabih Ghassemlooy, Stanislav Zvanovec, Luis Nero Alves, Mohammad Khalighi. Optimization and design of a diffuse optical wireless sensor network. *Applied optics*, 2022, 61 (22), pp.6599-6608. 10.1364/AO.463330. hal-04538763

**HAL Id: hal-04538763**

**<https://hal.science/hal-04538763v1>**

Submitted on 9 Apr 2024

**HAL** is a multi-disciplinary open access archive for the deposit and dissemination of scientific research documents, whether they are published or not. The documents may come from teaching and research institutions in France or abroad, or from public or private research centers.

L'archive ouverte pluridisciplinaire **HAL**, est destinée au dépôt et à la diffusion de documents scientifiques de niveau recherche, publiés ou non, émanant des établissements d'enseignement et de recherche français ou étrangers, des laboratoires publics ou privés.

# Optimization and Design of a Diffuse Optical Wireless Sensor Network

THOMAS KAMALAKIS,<sup>1,\*</sup> ZABIH GHASSEMLOOY,<sup>2</sup> STANISLAV ZVANOVEC,<sup>3</sup> LUIS NERO ALVES,<sup>4,5</sup> AND MOHAMMAD KHALIGHI,<sup>6</sup>

<sup>1</sup>Department of Informatics and Telematics, Harokopio University of Athens, Greece, GR17778

<sup>2</sup>Northumbria Communication Research Lab (NCRLab), Northumbria University, Newcastle upon Tyne, UK

<sup>3</sup>Department of Electromagnetic Field, Czech Technical University in Prague, Czech Republic

<sup>4</sup>Department of Electronics Telecommunications and Informatics

<sup>5</sup>University of Aveiro and the Instituto de Telecomunicações, Aveiro, Portugal

<sup>6</sup>Institut Fresnel, UMR CNRS 7249, Ecole Centrale Marseille, Marseille, France

\*[thkam@hua.gr](mailto:thkam@hua.gr)

**Abstract:** Wireless sensor networks (WSNs) are currently being deployed in everyday objects to collect and transmit information related to humidity, temperature, heartbeat, motion, etc. Such networks are part of the massive machine-type communication scenario (mMTC) within the fifth/sixth generation of wireless networks. In this paper, we consider the optimization and design of an optical WSN composed of multiple battery-powered sensor nodes based on light-emitting diode transmitters. Extending our previous work, we take into account both line-of-sight and diffuse light propagation, and show that in indoor scenarios, diffuse radiation can improve link availability under shadowing/blocking and extend battery life. In order to optimize the optical wireless link parameters, we use a machine-learning approach based on a genetic algorithm to ascertain the performance limits of the system. The presented results indicate that the proposed system is a viable wireless option for WSNs within the context of mMTC.

© 2024 Optica Publishing Group under the terms of the [Optica Publishing Group Publishing Agreement](#)

## 1. Introduction

The internet-of-things (IoT) [1] constitutes one of the main drivers for the information and communication technology (ICT) industry. The fifth generation (5G) wireless networks have identified massive machine-type communications (mMTC) as a key enabler, encompassing use cases where multiple low-power sensor nodes (SNs) sporadically transmit information at relatively low data rates. Typical examples include smart-grids [2], smart cities [3], infrastructure monitoring [4], asset tracking [5], healthcare [6] and others. Wireless sensor networks (WSNs) composed of spatially distributed SNs within 5G/6G networks come with ever-increasing demands for higher energy efficiency and longer life spans [7].

WSNs offer unique features of network scalability, distributed control, etc. A range of radio frequency (RF) wireless technologies have been developed for industrial applications [8] but encounter problems such as tight wireless bandwidth resources, increased crosstalk (especially in multi-hop scenarios [9]), easy signal interception, fading, and relatively low power efficiency. Optical wireless communications (OWC) covering the infrared [10] and visible [11] part of the spectrum are being considered as part of future 5G/6G enabling technologies in certain applications, where RF-based system is not the preferred option [12]. Typical applications include smart manufacturing [13], information proclaiming to the public [14], underwater IoT [15], intelligent transportation [16], agriculture [17] and smart health-care [18]. OWC-based WSN may offer higher data throughputs, inherent security, lower energy usage [13], [14]. However, due to the limitations of line-of-sight (LOS), energy-efficient network models and routing protocols must be used provided. In [19], an industrial monitoring system based on an optical camera communication system with an artificial neural network-based group detection mechanism for

46 industry applications was proposed and implemented. In [20] and [21] channel modeling and  
 47 characterization of indoor visible light communication for medical body-area networks were  
 48 investigated. In [22] a triple-hop underwater WSN based on the hybrid RF and OWC links  
 49 with the relay between the SNs and the access point was investigated by means of Monte-Carlo  
 50 simulation. In [23], energy harvesting and energy efficient modulation schemes for visible light  
 51 communications (VLC) in industrial applications were investigated.

52 In [24], we studied an indoor OWC-based WSN using a VLC down-link and an infrared (IR)  
 53 up-link to connect master nodes (MN) and SNs. The system under consideration is shown in  
 54 Figure 1. Figure 1a shows a number of SNs that are periodically sending sensor readouts to one or  
 55 multiple MNs using IR OWC up-links. The MN uses a VLC down-link to send acknowledgments  
 56 and coordinate transmissions. Light signals transmitted from the SN can reach the MN through  
 57 the LOS path or via multiple reflections from various surfaces of the room (diffuse path). Figure  
 58 1b shows the transceiver diagram. At the transmitter (TX), the sensor information modulates the  
 59 intensity of the IR LED(s) via the driver circuit. At the receiver (RX), an optical bandpass filter  
 60 is used for limiting the ambient light noise prior to optical-to-electrical conversion using a PIN  
 61 photodiode and a trans-impedance amplifier (TIA). In addition to the actual sensors, the node  
 62 contains a micro-controller unit (MCU), which coordinates the node data transmission cycle. The  
 63 MN architecture is similar except for exchanging the transmitting/receiving to use a LED-based  
 64 VLC system for simultaneous communication and illumination. Considering LOS contribution  
 65 only, one may obtain significant battery lifetimes.

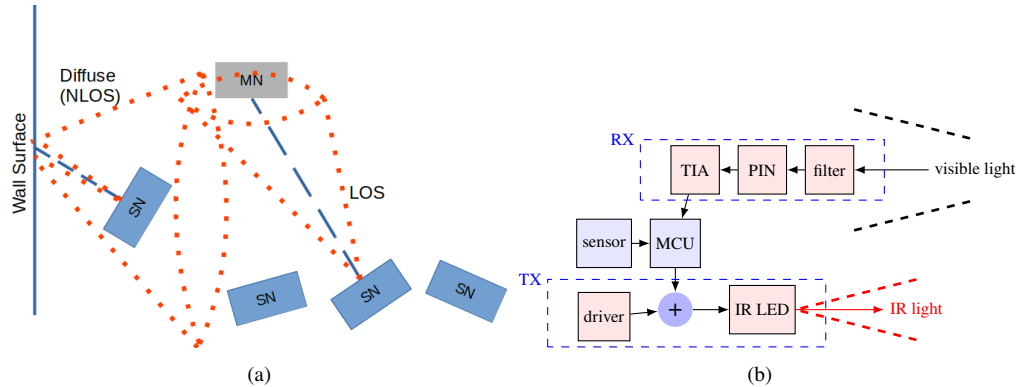


Fig. 1. (a) Hybrid VLC/IR network architecture (b) SN subsystem.

66 The contribution of the present work lies in several areas. First of all we provide a more realistic  
 67 system model accounting for the contribution of diffuse light resulting from beam reflections at  
 68 various room surfaces. For relatively high data-rate links, it is well known that such reflections  
 69 will result in inter-symbol interference (ISI) [25]. However, we use a ray tracing scheme to  
 70 show that the OWC channel can be considered approximately flat, for data rates considered in  
 71 typical IoT applications (of the order of kb/s). Therefore, at the MN receiver, diffuse radiation  
 72 simply adds up to the LOS component improving the signal-to-noise ratio (SNR). This implies  
 73 prolonged battery life.

74 Second, we provide an efficient diffuse power estimation scheme in order to quickly estimate  
 75 the link budget taking into account diffuse light contribution. Our approach is actually a simplified  
 76 version of the impulse response estimation model presented in [26]. Since the diffuse channel can  
 77 be considered flat, there is no need to track arrival times of the diffuse components and hence the  
 78 power estimation is considerably simplified requiring much less computational time and memory  
 79 resources.

80 Third, we adopt a machine-learning approach based on a specially modified genetic algorithm

81 (GA) [27] in order to optimize link design in terms of battery life. Using established full  
 82 ray-tracing schemes would render such optimizations impractical. Our simplified link budget  
 83 model discussed above however, renders such optimizations feasible. Various parameters are  
 84 included in the optimization pertinent to the SN/MN arrangement, etc taking into account the  
 85 indoor environment (wall configuration, surface reflectivity, etc). To our knowledge, this kind of  
 86 optimization has not been previously undertaken in the literature.

87 A fourth area of contribution is the fact that, as evidenced by the obtained results, the battery  
 88 life times of the SNs are considerable, indicating the potential of optical wireless for WSNs. We  
 89 pay special attention to scenarios where no LOS power is received (e.g. due to blocking) and  
 90 show that optimizing the transmitter beam-width can lead to significant power savings. Our  
 91 results can therefore pave the way for adopting optical technologies in the context of WSNs  
 92 and IoT. And last but not least, the full link and energy consumption models and optimization  
 93 engine of our proposed approach, implemented in `Python` is freely made available under an  
 94 open-source license [28].

95 The rest of the paper is organized as follows: Section 2 describes the model used to develop  
 96 the OWC link and energy usage for the application scenario at hand. Using ray-tracing we show  
 97 that in typical indoor conditions, the diffuse channel is flat and outlines how the diffuse power can  
 98 be efficiently calculated. For a target up-link bit error rate (BER) we can therefore estimate the  
 99 required transmission power and driving current at the LED of the SN. Given the transmission  
 100 cycle of the SN, this information can also be used to estimate the battery life. The model of  
 101 Section 2 feeds a GA in order to optimize the battery life of the SNs. This algorithm is outlined  
 102 in Section 3. Section 4 presents the results obtained and their impact on WSN-based applications.  
 103 Section 5 concludes the paper providing a research outlook.

## 104 2. System Model

105 We consider two rooms of different dimensions as outlined in Table 1. Configuration A is a small  
 106 room and is identical to the one considered in [26], whereas configuration B is a larger room  
 107 indicative of office spaces, storage rooms, etc. The reflectivity values in Table 1 correspond to  
 108 typical white paint on plasterboard or acoustic tiles for the sidewalls/ceiling and light gray tiles  
 109 for the floor.

### 110 2.1. Optical wireless channel

111 The OWC channel is a linear, time invariant (LTI) system described by its impulse response  $h(t)$ .  
 112 The LOS contribution is described by a Dirac delta function  $h_{\text{MN}}\delta(t - t_{\text{MN}})$  [26], where  $h_{\text{MN}}$   
 113 is the LOS channel gain,  $t_{\text{MN}} = R_{\text{MN}}/c$  the propagation delay between the SN and the MN,  $R_{\text{MN}}$   
 114 their distance and  $c$  the speed of light. The total impulse response  $h(t)$  equals the sum of the  
 115 LOS and the diffuse light component  $h_{\text{D}}(t)$ , i.e.:

$$h(t) = h_{\text{MN}}\delta(t - t_{\text{MN}}) + h_{\text{D}}(t) \quad (1)$$

116 We use an in-house `Python` implementation of the modified Monte Carlo ray-tracing method [29]  
 117 to obtain  $h_{\text{D}}(t)$  and then use the fast Fourier transform (FFT) to determine the diffuse channel  
 118 frequency response  $H_{\text{D}}(f) = \mathcal{F}\{h_{\text{D}}(t)\}$ , where  $\mathcal{F}\{\cdot\}$  denotes the Fourier transform. We  
 119 assume purely diffusive ideal Lambertian reflectors.

120 Figure 2 shows  $H_{\text{D}}(f)$  obtained for the up-link for configurations A and B of Table 1  
 121 and for MN positioned in the middle of the ceiling,  $\mathbf{r}_{\text{MN}} = [L/2, W/2, H]$  while the SN is  
 122 positioned at two different locations along the floor diagonal:  $\mathbf{r}_{\text{SN}} = \mathbf{r}_1 = [L/2, W/2, 0]$  and  
 123  $\mathbf{r}_{\text{SN}} = \mathbf{r}_2 = [L/4, W/4, 0]$ . The SN and MN are directed according to Table 1. Figure 2a,  
 124 corresponding to configuration A, shows that for both SN positions,  $H_{\text{D}}(f)$  varies in the MHz-  
 125 range and can therefore be considered effectively flat in the sub-MHz frequency range. The half

Table 1. Simulation parameters

Parameter	Config. A	Config. B
Length, $L$	5 m	10 m
Width, $W$	5 m	10 m
Height, $H$	3 m	4 m
Window height, $H_w$	1 m	2 m
Window width, $W_w$	1 m	2 m
Peak spectral irradiance, $p_n$	2 W/nm/m <sup>2</sup>	
Ambient light temperature, $T_K$	5800 K	
Wall reflectivity, $\rho_w$	0.8	
Ceiling reflectivity, $\rho_c$	0.8	
Floor reflectivity, $\rho_f$	0.3	
MN field-of-view, $FOV_{MN}$	$\pi/2$	
SN field-of-view, $FOV_{SN}$	$\pi/2$	
MN orientation, $\mathbf{n}_{MN}$	$\hat{\mathbf{z}}$	
SN orientation, $\mathbf{n}_{SN}$	$-\hat{\mathbf{z}}$	
MN transmission power, $P_{MN}$	6 W	
Maximum SN transmission power, $P_{SN}$	25 mW	
IR LED half intensity angle, $\Phi_{1/2}$	60°	
IR LED pattern order, $m$	1	
IR LED driver curve	TSFF5210 [24]	
Max SN driver current, $I_{max}$	100 mA	
Responsivity model	BPV10NF [24]	
VLC rejection filter model	VTB5051BH [24]	
IR rejection filter model	BPV10NF [24]	
Maximum data rate, $R_{max}$	10 kb/s	
Target error rate, $BER_0$	$10^{-3}$	
Spectral efficiency, $\eta_{eff}$	0.4 bit/s/Hz	
Up-link message length, $L_u$	200 bits	
Down-link message length, $L_d$	200 bits	
Feedback resistance, $R_F$	1 M $\Omega$	
Modulation type	OOK	
RMS voltage noise density, $V_{rms}$	15 nV/ $\sqrt{\text{Hz}}$	
RMS current noise density, $V_{rms}$	400 fA/ $\sqrt{\text{Hz}}$	
Voltage noise corner frequency, $f_{cv}$	1 kHz	
Current noise corner frequency, $f_{ci}$	1 kHz	
Sleep mode current, $I_{SL}$	400 nA	
Wake-up current, $I_{WU}$	1.3 mA	
Read out current, $I_{RO}$	1.3 mA	
Wake-up time, $t_{WU}$	20 ms	
Read-out time, $t_{RO}$	40 ms	
Cycle period, $t_{CY}$	1 min	
Battery capacity, $Q_{TOT}$	220 mAh	

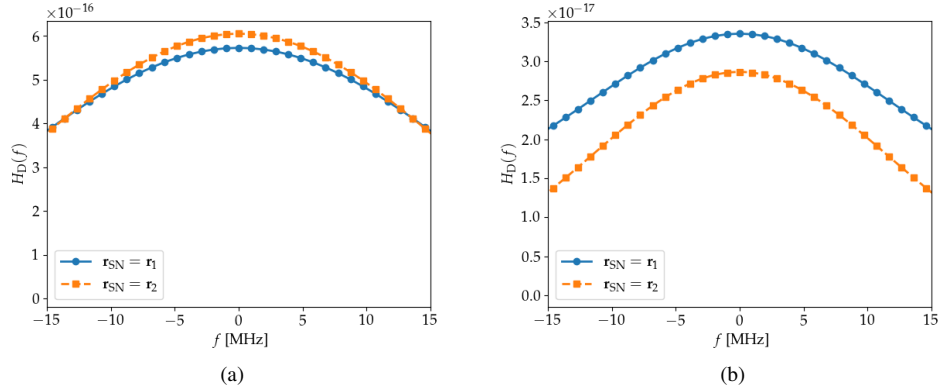


Fig. 2. Diffuse channel impulse response  $|H_D(f)|$  for (a) configuration A and (b) configuration B.

126 width 1 dB bandwidth  $B_{1\text{dB}}$  values of  $|H_D(f)|^2$  are 8.2 and 7.3 MHz for  $\mathbf{r}_{\text{SN}} = \mathbf{r}_1$  and  $\mathbf{r}_{\text{SN}} = \mathbf{r}_2$   
 127 respectively. A similar behavior is obtained for configuration B, where  $B_{1\text{dB}}$  is now 7.2 and 5.3  
 128 MHz for  $\mathbf{r}_{\text{SN}} = \mathbf{r}_1$  and  $\mathbf{r}_{\text{SN}} = \mathbf{r}_2$ , respectively. These results indicate that the diffuse channel can  
 129 be considered flat for WSN applications and can therefore be described by a scalar channel gain  
 130  $h'_{\text{MN}}$ . The total channel gain will simply be equal to the sum of the LOS and diffuse channel  
 131 gains:

$$h_{\text{MN}}^{\text{TOT}} = h_{\text{MN}} + h'_{\text{MN}} \quad (2)$$

132 where

$$h'_{\text{MN}} = \int_{-\infty}^{+\infty} h_D(t) dt \quad (3)$$

133 There are two basic aspects of the physical layer model that we present in this section: the  
 134 channel model discussed in subsection 2.2 and the transceiver model discussed in subsection 2.3  
 135 which includes power consumption.

### 136 2.2. Diffuse power and link budget

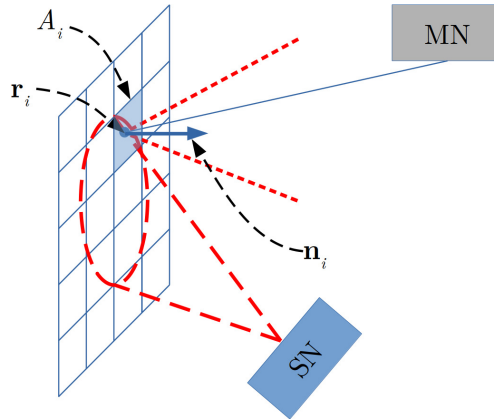


Fig. 3. Estimation of the diffuse light channel gain.

137 Assuming a generalized Lambertian-type TX of order  $m$ , located at  $\mathbf{r} = \mathbf{r}_S$ , oriented along the  
 138 unitary vector  $\mathbf{n}_S$ , and a receiver placed at  $\mathbf{r} = \mathbf{r}_R$ , which is oriented along  $\mathbf{n}_R$  and effective area  
 139  $A_R$  and field-of-view equal to FOV, the channel gain is determined by:

$$h(\mathbf{r}_R, \mathbf{n}_R, \mathbf{r}_S, \mathbf{n}_S) = \frac{m+1}{2\pi R^2} \cos^m \phi \cos \theta A_R U\left(\frac{\theta}{\text{FOV}}\right) \quad (4)$$

140 where

$$\cos \theta = \frac{\mathbf{n}_R \cdot (\mathbf{r}_S - \mathbf{r}_R)}{R} \quad (5a)$$

$$\cos \phi = \frac{\mathbf{n}_S \cdot (\mathbf{r}_R - \mathbf{r}_S)}{R} \quad (5b)$$

$$R = |\mathbf{r}_S - \mathbf{r}_R| \quad (5c)$$

143 As part of our optimizations and in order to avoid adopting time-consuming ray-tracing schemes  
 144 as in Section 2.1, we use a faster simulation method, where all room surfaces are represented by  
 145 a collection of elementary sub-surfaces  $A_i$ , as shown in Figure 3. We first calculate the incident  
 146 power  $P_i^{(1)}$  on each  $A_i$  from the SN using (4), i.e., at the first light bounce. We also calculate  
 147 the intra-subsurface LOS gain  $h_{qp}$  assuming  $A_p$  and  $A_q$  are the TX and RX, respectively. For  
 148  $A_p$ , the transmitted power is  $r_p P_p^{(0)}$ , where  $r_p$  is the reflectivity of  $A_p$ . Following the second  
 149 bounce, the power received by  $A_q$  is written as the sum of powers received by all other elementary  
 150 surfaces. More generally, the power received at the  $b^{\text{th}}$  bounce is given by:

$$P_q^{(b)} = \sum_{p=1}^{N_E} h_{qp} r_p P_p^{(b-1)} \quad (6)$$

151 In (6),  $N_E$  is the number of elementary surfaces within the room. If  $h_q^{\text{MN}}$  are the channel gains  
 152 assuming  $A_q$  is the TX and MN the RX, then the diffuse-light power  $P_D^{(b)}$  is the sum of the  
 153 received power from all  $A_q$  and therefore, the total diffuse power is given as:

$$P_D = \sum_{b=1}^{N_B} P_D^{(b)} = \sum_{b=1}^{N_B} \sum_{q=1}^{N_E} h_q^{\text{MN}} r_q P_q^{(b)} \quad (7)$$

154 where  $h_q^{\text{MN}}$  is the channel gain between  $A_q$  and the MN. Using (6) and (7) is analogous to the  
 155 impulse response estimation adopted in [26], except that the channel here is considered to have  
 156 flat response, and hence we simply add power contributions from consecutive bounces, speeding  
 157 up computations significantly.

158 Assuming the SN is positioned on various points along the diagonal  $\mathbf{r}_{\text{SN}} = [x, x, 0]$  and its  
 159 orientation is vertical, i.e.  $\mathbf{n}_{\text{SN}} = \hat{\mathbf{z}}$ , we have investigated the power distribution profiles  $P_D^{(b)}$  in  
 160 Figure 4a for configuration B. Interestingly enough, the power for  $b = 1$  is smaller than  $b = 2$ .  
 161 For  $b = 1$ , most of the IR power illuminates the ceiling elements and therefore lies outside the  
 162 field-of-view (FOV) of the MN. For  $b = 2$ , the MN captures optical power from sidewall elements  
 163 that are now illuminated by the ceiling. Figure (4b), depicts the power distribution profiles for  
 164 the LOS and diffuse paths, as well as the total power level for configuration B. Note that, near the  
 165 center of the diagonal ( $x \cong L/2$ ), the LOS path is much stronger than the diffuse path. This is  
 166 because at  $x \cong L/2$ , the alignment is optimal, since both  $\mathbf{r}_{\text{SN}}$  and  $\mathbf{r}_{\text{MN}}$  lie on the line between the  
 167 transceivers. Near its edges of the room, the diffuse component contributes greatly to the total  
 168 received power, since alignment is worse.

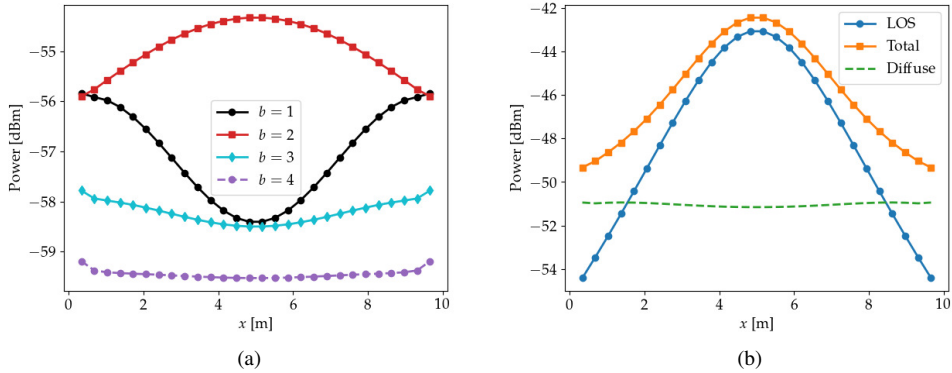


Fig. 4. a) Diffuse power contribution depending on bounce  $b$  and b) comparison of propagation path contribution to the received power.

### 169 2.3. Transceiver model and energy efficiency

170 The transceiver model includes the transmission spectra of nodes, RX filter spectra, photodiode  
 171 responsivity, ambient light noise and TIA noise. Here we briefly describe the model features and  
 172 the interested reader is referred to [24] for an in-depth analysis.

173 The SN transceiver is modeled based on the characteristics of the TSFF5210 IR LED and the  
 174 VTB5051BH silicon photodiode with an IR rejection filter (Table 1). The IR LED transmission  
 175 spectra  $S_T(\lambda)$  is described by a Gaussian profile with a full width at half maximum (FWHM) of  
 176  $\Delta\lambda = 40$  nm, peaking around  $\lambda = 870$  nm. The optical power-current characteristic  $P_T = f(I_D)$   
 177 is obtained by polynomial fitting of the actual light-current curve of TSFF5210. We assume a  
 178 super-Gaussian profile for the IR rejection filter of order 3 with a 10dB bandwidth of 230 nm  
 179 peaking at 435 nm while the responsivity  $\mathcal{R}(\lambda)$  of the detector is described by a polynomial with  
 180 respect to  $\lambda$  with coefficients extrapolated by curve-fitting from the BPV10NF responsivity.

181 The MN transceiver is modeled based on typical spectra of warm white phosphorescent LEDs.  
 182 We describe the transmission spectra using a sum of two Gaussian profiles, corresponding to  
 183 the blue and the phosphor components peaking at 470 and 600 nm, respectively, with FWHM  
 184 equal to 20 and 100 nm, respectively. The daylight blocking filter is described by a 3rd order  
 185 super-Gaussian peaking at 870 nm with a 10dB bandwidth of 300 nm. Given the spectral  
 186 properties of the transceiver, we determine the effective responsivity  $\mathcal{R}_{\text{eff}}$  describing the matching  
 187 between the transmission spectra, the receiver's rejection filter and responsivity. Following  
 188 the approach of [24], we obtain 0.49A/W and 0.32A/W for  $\mathcal{R}_{\text{eff}}$  in the up-link and down-link,  
 189 respectively.

190 The RX noise is mainly due to the ambient light-induced shot noise and the TIA thermal noise,  
 191 where the former is usually dominant and can be characterized by its spectral irradiance, which  
 192 in our model follows a black-body radiation model with an absolute temperature of 5800 K.  
 193 Given the position and orientation of the emitting surfaces (e.g. windows), (4) can be modified  
 194 to estimate the ambient light power incident at the RX. We assume a 1 and 4 m<sup>2</sup> window for  
 195 configurations A and B, respectively, (Table 1) with peak spectral irradiance of 2 W/nm/m<sup>2</sup>. We  
 196 note that  $\mathcal{R}_{\text{eff}}$  for ambient light is 0.09A/W for the MN and 0.13A/W for the SN [24]. Assuming  
 197 on/off keying (OOK) modulation, then for a given SNR the transmit power  $P_T$  and thus the LED  
 198 drive current  $I_D$  can be determined. The energy usage at the SN can be calculated considering  
 199 the currents drawn by the transceiver and the MCU during various phases. Table 1 quotes typical  
 200 values for each cycle [24]. Based on these, we can calculate the charge  $Q_{\text{CY}}$  drawn from the  
 201 battery at each cycle and determine the node battery life-time  $t_{\text{BL}}$  given the battery capacity



202  $Q_{\text{TOT}}$  (assumed 220 mAh, typical of a coin-cell battery).

203 **3. Link Optimization**

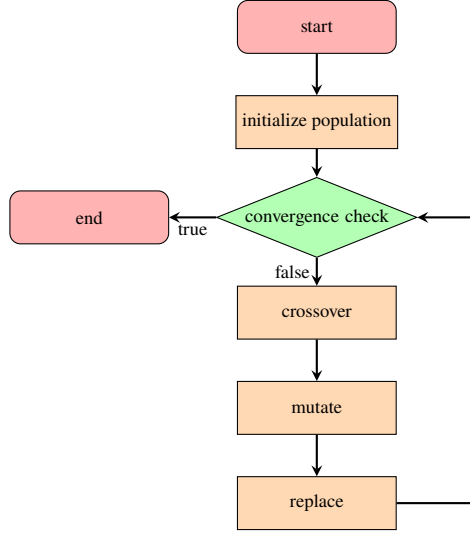


Fig. 5. The flowchart of the genetic algorithm used in this work.

204 In Figure 5, we show the flowchart of the GA used to optimize the system parameters such as  
 205 the SN orientation and data rate. Initially, we randomly choose a population consisting of  $N_{\text{INIT}}$   
 206 realizations of the system (chromosomes). The algorithm then proceeds to select candidates, by  
 207 generating offsprings using a *crossover* operation, which transfers part of the parent genes to the  
 208 offsprings. The genes of the offsprings are also *mutated*, i.e. randomly changed in an attempt to  
 209 increase diversity. If a chromosome is produced that is stronger than the weakest chromosome  
 210 in the existing pool, then the former chromosome is replaced by the latter. We then carry out  
 211 a convergence check to see whether the algorithm’s termination criteria are met and if not, we  
 212 repeat the previous steps.

213 In each iteration, the strongest 50 % of the chromosomes constitute the mating pool. We  
 214 choose two parents through tournament selection and we calculate the offspring using uniform  
 215 crossover, which consists of tossing an unbiased coin and randomly selecting the value of each  
 216 offspring gene from either the first or the second parent. The mutation is achieved by adding a  
 217 random correction factor  $\Delta v_k$  to each of the offspring genes  $v_k$ . The corrections are determined  
 218 by  $\Delta v_k = \alpha \beta_k v_k$ , where  $0 \leq \alpha \leq 1$  is the *mutation factor*, and  $\beta_k$  are randomly chosen from a  
 219 uniform distribution inside  $[-1, 1]$ . The chromosome values considered for the optimization  
 220 are the inclination and azimuth angles  $\theta$  and  $\phi$ , respectively, as well as the data rate  $R_b$ . The  
 221 angles determine the orientation of the SN,  $\mathbf{n}_{\text{SN}} = [\cos \phi \sin \theta, \sin \phi \sin \theta, \cos \theta]$ , while  $R_b$   
 222 is related to the required bandwidth  $B$  and the transmission time  $t_{\text{TX}}$ . Note that, the strength of  
 223 each chromosome is determined by a fitness function. In our case, we let the battery life  $t_{\text{BL}}$   
 224 determine the fitness of each system in order to optimize the energy efficiency at the SN. It is  
 225 important to ensure that the maximum driving current should not exceed a specified value  $I_{\text{max}}$   
 226 due to the LED specifications, see Table 1. If this condition is not met, we set the fitness value  
 227 equal to zero to avoid a non-viable solution.

228 The overall model including the GA which is available under an open-source license [28], is  
 229 implemented in Python using standard libraries such as `numpy`, `scipy` and `matplotlib`.  
 230 In order to speed-up the code execution, we choose to rely on vectorization, avoiding loops as

231 much as possible. For example, it is much more efficient to determine all intra-channel gains  $h_{qp}$   
 232 simultaneously using a vector/matrix approach. In addition we only need to calculate  $h_{qp}$  once,  
 233 since they only depend on the positioning and orientation of the sub-surfaces  $A_q$ . This speeds up  
 234 the fitness evaluations considerably. In our simulations we also took advantage of Python's  
 235 multiprocessing package to distribute computations in multiple processes.

#### 236 4. Results and Discussions

237 In the proposed optimization scheme, we seek to determine the optimal values of  $[\phi, \theta, R_b]$   
 238 for every position in the floor diagonal  $\mathbf{r}_{SN} = [x, x, 0]$ . We examine three cases: in the first  
 239 and second variations, we only account for either the LOS or diffuse light power, respectively,  
 240 when calculating  $t_{BL}$ . In the third variation, we sum up both contributions. The population  
 241 has  $N_{INIT} = 50$  chromosomes and we use a mutation factor  $\alpha = 0.1$ . The algorithm terminates  
 242 when either a maximum number of crossovers occurs (in our case 20000) or the population's  
 243 fitness values  $f_i$  do not differ significantly from each other. We measure the population fitness  
 244 smoothness  $S = (f_{max} - f_{min})/f_{max}$  where  $f_{max}$  and  $f_{min}$  are the maximum and minimum values  
 245 of population fitnesses respectively. We terminate the algorithm if  $S < 0.05\%$ .

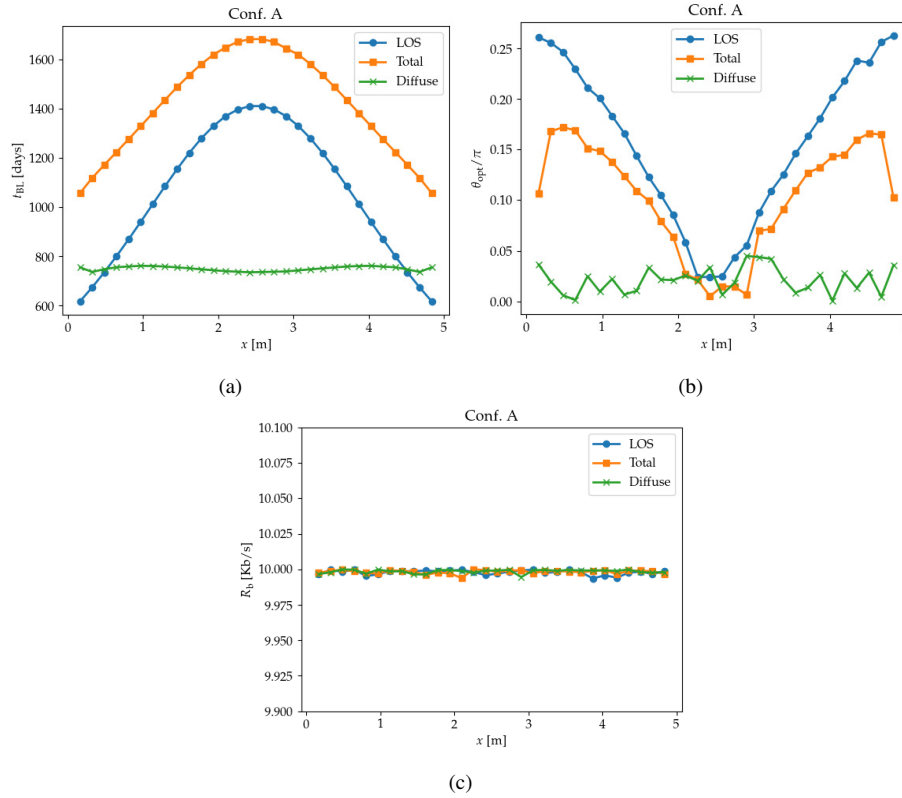


Fig. 6. Optimization results for room configuration A: a) battery lifetime, b) optimal elevation angle and c) optimal data rate

246 Figure 6a depicts the fitness function (i.e.  $t_{BL}$ ) across the diagonal of the room  $[x, x, 0]$   
 247 obtained by the GA for configuration A assuming LOS, diffuse and combination of both. It is  
 248 interesting to note that the LOS component  $t_{BL}$  is symmetrical around 2.5 m with a peak value of  
 249 1400 days dropping at a rate of 400 day/m compared to the diffuse, which is almost flat at 750 day

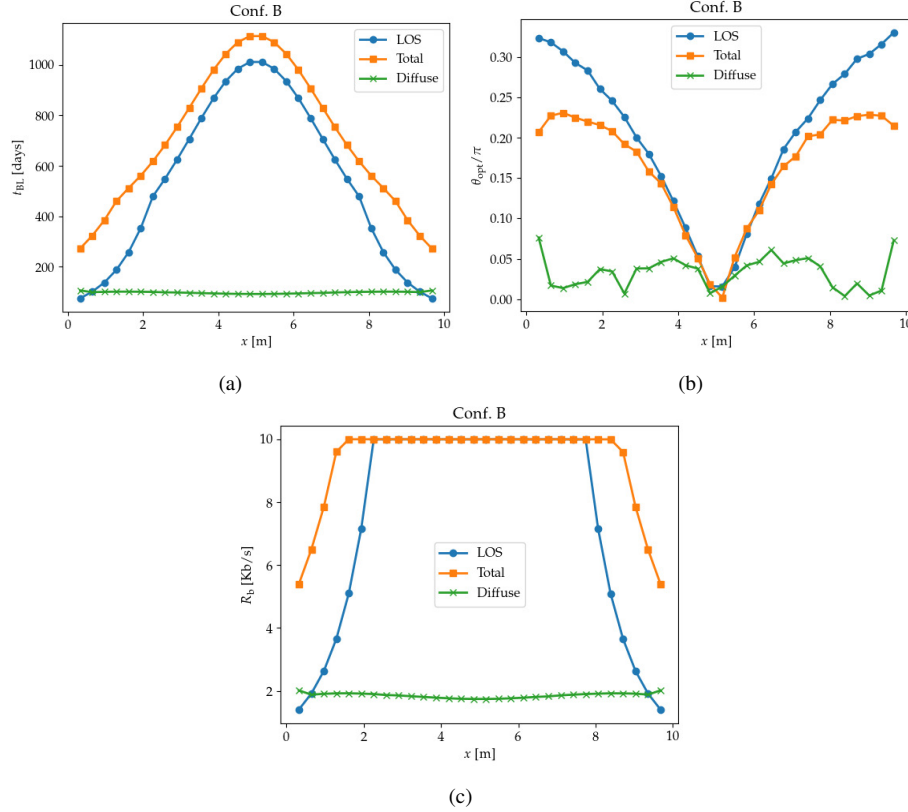


Fig. 7. Optimization results for room configuration B: a) battery lifetime, b) optimal elevation angle and c) optimal data rate

250 for the  $0 \leq x \leq 5$  m. This is due to the fact that as the MN/SN distance is increased, the power  
 251 budget worsens. Considering both LOS and diffuse components, energy efficiency is improved  
 252 particularly near the edges of the diagonal. Figures 6b and 6c show the optimal elevation angle  
 253  $\theta$  and the data rate  $R_b$ . For LOS, the optimal  $\theta$  increases when we move away from the center  
 254 ( $x = 2.5$  cm) to better align with the MN, whereas the diffuse scenario favors  $\theta \approx 0$ , in which  
 255 case the SN is almost pointing directly upwards,  $\mathbf{n}_{SN} \approx \hat{\mathbf{z}}$ . The obtained data rate is given by  
 256  $R_b \approx 10$  kb/s =  $R_{max}$ , which is the maximum allowable value given by system constraints. The  
 257 fact that high  $R_b$  are favored can be explained through the RX electrical SNR in the case of OOK,  
 258 given as:

$$\text{SNR} = \frac{R_{\text{eff}}^2 P_R^2}{2\sigma^2} \quad (8)$$

259 where  $P_R$  is the received optical signal power (proportional to the transmit power  $P_T$ ) and  $\sigma^2$  is  
 260 the RX noise power. Neglecting the TIA noise, we have  $\sigma^2 = 2qI_{\text{amb}}B$ , where  $I_{\text{amb}}$  is the DC  
 261 current due to ambient light,  $q$  is the electron charge,  $B = R_b/\eta_{\text{eff}}$  the signal bandwidth and  $\eta_{\text{eff}}$   
 262 the spectral efficiency. Thus, with reference to (8),  $P_T \propto \sqrt{R_b}$ . Assuming linear light-current  
 263 characteristic at the SN LED, we can also deduce that  $I_D \propto \sqrt{R_b}$ . Since the duration of the  
 264 transmission phase  $t_{TX}$  is proportional to the bit duration  $1/R_b$ , we readily see that the charge  
 265 drawn from the node battery is  $Q_{TX} \propto 1/\sqrt{R_b}$ . This implies that provided that  $I_D \leq I_{\text{max}}$ ,  
 266 increasing  $R_b$  leads to better energy efficiency.

267 Figure 7, shows the optimized results for configuration B. As shown in Figure 7a, the diffuse

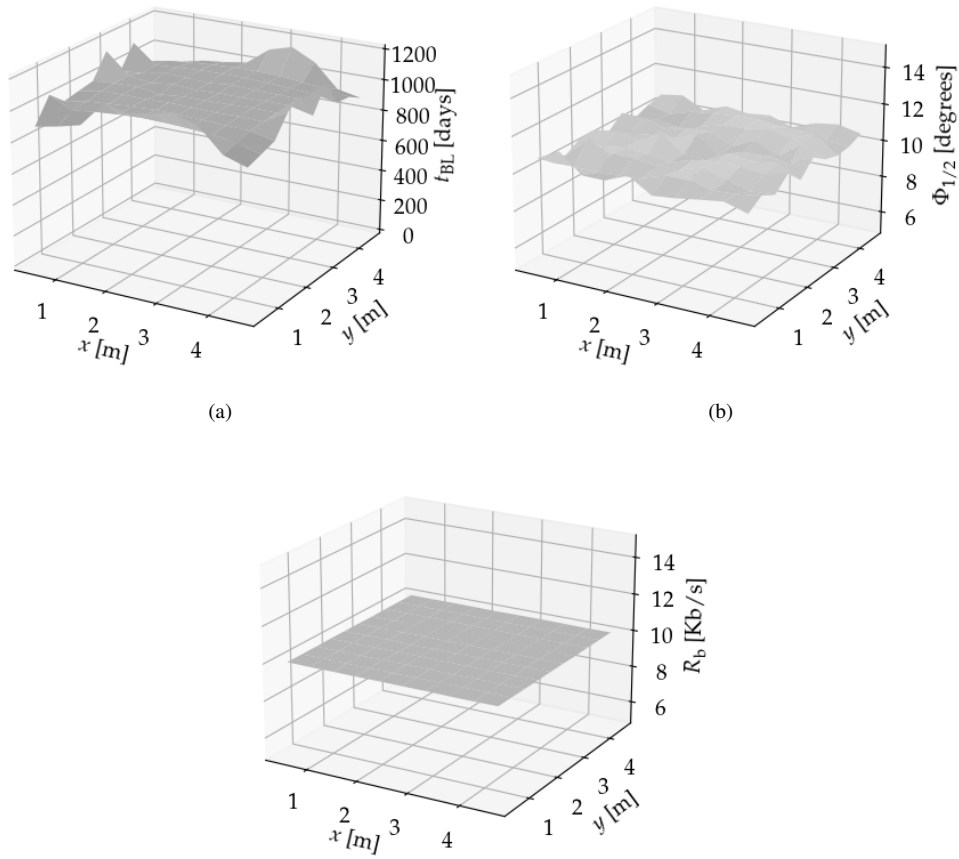


Fig. 8. Optimization results for diffuse light propagation configuration A: a)  $t_{BL}$ , b)  $\Phi_{1/2}$  and c)  $R_b$ .

268 path offers the lowest battery lifetime with an average of  $\approx 96$  days. However it can still increase  
 269 the overall battery lifetime considerably, especially at the edges of the diagonal. The optimal  
 270 elevation angles exhibit a similar variation as those in Figure 6b, implying that if the diffuse  
 271 component alone is considered the optimal SN orientation is still  $\mathbf{n}_{SN} \approx \hat{\mathbf{z}}$ . As expected, the  
 272 optimal SN elevation angles increase with the distance from floor center, in order to improve  
 273 SN/MN alignment. Figure 7c depicts the optimal data rate, which is not always  $\approx 10$  kb/s since  
 274 the required driving current must not exceed  $I_{max}$ . Considering only the diffuse component, the  
 275 optimal  $R_b \approx 2$  kb/s. For the LOS component,  $R_b$  is much higher except for the points near the  
 276 edge of the diagonal. Assuming both contributions from LOS and diffuse paths, we obtain an  
 277 optimal data rate  $\geq 5$  kb/s for all SN positions considered (orange curve in Figure 7c).

278 For the LOS path, an obvious way to improve link budget is to choose a smaller beam-width  
 279  $\Phi_{1/2}$  thereby reducing beam spreading at the expense of tighter alignment control and limited  
 280 mobility. It is interesting to investigate the optimal beam pattern for the diffuse path as well  
 281 considering many possible positions for the SN. Figures 8 and 9, show the results for the two room  
 282 configurations assuming that the beam-width  $\Phi_{1/2}$  is also included in the optimization inside  
 283 a range of  $[10^\circ, 20^\circ]$ . Figures 8a, 8b and ?? depict the values of  $t_{BL}$ ,  $\Phi_{1/2}$  and  $R_b$  respectively

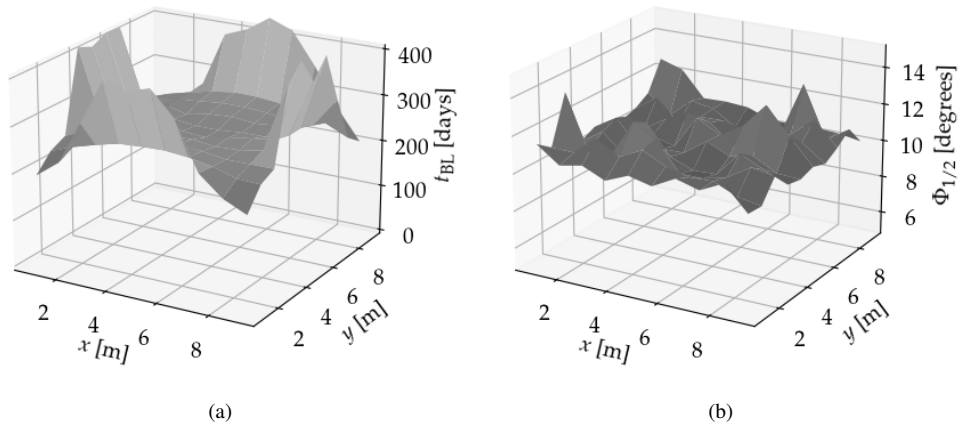


Fig. 9. Optimization results for diffuse light propagation configuration B: a)  $t_{BL}$ , b)  $\Phi_{1/2}$  and c)  $R_b$ .

284 obtained for configuration A, assuming a  $10 \times 10$  grid on the floor of the room. A minimum  
 285 value of  $t_{BL}$  obtained was 890 days at the room corners. The optimal value for  $\Phi_{1/2}$  was near  
 286  $10^\circ$ . This does not change even if we widen the allowed range for  $\Phi_{1/2}$  in the GA, indicating a  
 287 non-directed scenario where a tight beam impinges on the nearby room sidewall and light reaches  
 288 the MN by a diffuse path. For all SN positions considered, the optimal  $R_b$  obtained is  $\cong 10$  kb/s.  
 289 The results for configuration B are shown in Figure 9. In this case the minimum value of  $t_{BL}$  is  
 290 186 days and is maximized near the sidewalls reaching up to 450 days. Again, the algorithm  
 291 favors beam-widths near  $10^\circ$  while the optimal data rate ranges from 3.6 kb/s to 9.4 kb/s.

## 292 5. Conclusions and future directions

293 In this work, we took a deeper look in the potential of optical technologies for WSNs and IoT  
 294 applications which are relevant within 5G and beyond mMTC applications. We presented a  
 295 realistic model of describing a hybrid VLC/IR WSN, which included diffuse-light propagation.  
 296 We showed that for typical data rates considered in most indoor mMTC applications, the diffuse  
 297 channel can be considered flat. This allowed us to implement an efficient link budget model

298 that can be used to significantly speed up computations in system optimizations. To maximize  
299 battery life, we used a machine learning approach based on a GA to optimize the MN/SN  
300 configurations and showed that significant SN battery lifetimes can be obtained even for coin-cell  
301 battery capacities. We also investigated scenarios where only the diffuse light contribution was  
302 considered in the optimization and with the SN TX beam-width was considered as an optimization  
303 parameter. For data rates envisioned in such applications, diffuse light propagation can improve  
304 the up-link power budget and improve energy efficiency. This is true for both small and larger  
305 room configurations such as the ones examined in this work. The optimizations show that when  
306 the LOS path is blocked, the diffuse channel actually favors non-directed configurations with  
307 narrower beam-widths where the IR light is aimed at the room's sidewalls, reaching the MN via  
308 single and multiple bounces. Both our model and our optimization engine are available freely on  
309 the web under an open-source license for other researchers to use.

310 The results obtained in this paper point towards some interesting research directions to  
311 implement VLC/IR WSNs. A key question is whether the SN configuration can be changed  
312 in an adaptive manner. One could envision controlling the IR LED radiation pattern using  
313 micro-electromechanical systems [30] while the direction of transmission could be also be  
314 controlled by low-cost servo-motors mounted at the SN. It would also be interesting to develop  
315 algorithms for the real-time optimization of up-link performance that can converge quickly in  
316 order to limit power dissipation during the optimization stage. Another interesting scenario  
317 would be to investigate multi-hop scenarios where SNs, which are far from the MN or their LOS  
318 path can be blocked, communicate with the MN via other SNs to send reading to the MN. It is  
319 our intend to investigate some of these research questions in future research works.

320 **Funding.** This publication was based upon work from COST Action NEWFOCUS CA19111, supported  
321 by COST (European Cooperation in Science and Technology)

## 322 References

- 323 1. S. Nižetić, P. Šolić, D. L.-d.-I. González-de, L. Patrono *et al.*, "Internet of things (iot): Opportunities, issues and  
324 challenges towards a smart and sustainable future," *J. Clean. Prod.* **274**, 122877 (2020).
- 325 2. H. C. Leigou, T. Zahariadis, L. Sarakis, E. Tsampasis, A. Voulkidis, and T. E. Velivassaki, "Smart grid: a demanding  
326 use case for 5g technologies," in *2018 IEEE International Conference on Pervasive Computing and Communications  
327 Workshops (PerCom Workshops)*, (IEEE, 2018), pp. 215–220.
- 328 3. R. Giuliano, F. Mazzenga, and A. Vizzarri, "Satellite-based capillary 5g-mmtd networks for environmental  
329 applications," *IEEE Aerosp. Electron. Syst. Mag.* **34**, 40–48 (2019).
- 330 4. F. Franchi, F. Graziosi, A. Marotta, and C. Rinaldi, "Structural health monitoring over 5g urllc network," in *European  
331 Workshop on Structural Health Monitoring*, (Springer, 2020), pp. 60–68.
- 332 5. S. Horsmanheimo, J. Säe, T. Jokela, L. Tuomimäki, E. Nigussie, A. Hjelt, S. Huilla, T. Dönmez, N. Le Bail, and  
333 M. Valkama, "Remote monitoring of iot sensors and communication link quality in multisite mmtd testbed," in  
334 *2019 IEEE 30th Annual International Symposium on Personal, Indoor and Mobile Radio Communications (PIMRC)*,  
335 (IEEE, 2019), pp. 1–7.
- 336 6. B. Wang, Y. Sun, C. Yuan, and X. Xu, "Lesla: A smart solution for sdn-enabled mmtd e-health monitoring system," in  
337 *Proceedings of the 8th ACM MobiHoc 2018 Workshop on Pervasive Wireless Healthcare Workshop*, (2018), pp. 1–6.
- 338 7. W. Saad, M. Bennis, and M. Chen, "A vision of 6g wireless systems: Applications, trends, technologies, and open  
339 research problems," *IEEE network* **34**, 134–142 (2019).
- 340 8. X. Li, D. Li, J. Wan, A. V. Vasilakos, C.-F. Lai, and S. Wang, "A review of industrial wireless networks in the context  
341 of industry 4.0," *Wirel. networks* **23**, 23–41 (2017).
- 342 9. H. Aslanyan and J. Rolim, "Interference minimization in wireless networks," in *2010 IEEE/IFIP International  
343 Conference on Embedded and Ubiquitous Computing*, (IEEE, 2010), pp. 444–449.
- 344 10. J. M. Kahn and J. R. Barry, "Wireless infrared communications," *Proc. IEEE* **85**, 265–298 (1997).
- 345 11. H. Haas, L. Yin, Y. Wang, and C. Chen, "What is lifi?" *J. lightwave technology* **34**, 1533–1544 (2016).
- 346 12. L. Bariah, L. Mohjazi, S. Muhaidat, P. C. Sofotasios, G. K. Kurt, H. Yanikomeroglu, and O. A. Dobre, "A  
347 prospective look: Key enabling technologies, applications and open research topics in 6g networks," *IEEE access* **8**,  
348 174792–174820 (2020).
- 349 13. M. Müller, D. Behnke, P.-B. Bök, C. Kottke, K. L. Bober, and V. Jungnickel, "Leverage lifi in smart manufacturing,"  
350 in *2020 IEEE Globecom Workshops (GC Wkshps)*, (IEEE, 2020), pp. 1–6.
- 351 14. V. Jungnickel, M. Hinrichs, K. Bober, C. Kottke, A. Corici, M. Emmelmann, J. Rufo, P.-B. Bök, D. Behnke, M. Riege  
352 *et al.*, "Enhance lighting for the internet of things," in *2019 Global LIFI Congress (GLC)*, (IEEE, 2019), pp. 1–6.

- 353 15. G. Schirripa Spagnolo, L. Cozzella, and F. Leccese, "Underwater optical wireless communications: Overview,"  
354 *Sensors* **20**, 2261 (2020).
- 355 16. X. Chen, J. Ding, B. Yu, H. Ma, and H. Lai, "A survey on wireless optical its for smart city," in *Asia Communications*  
356 *and Photonics Conference*, (Optical Society of America, 2019), pp. M4A–110.
- 357 17. Y. Mekonnen, S. Namuduri, L. Burton, A. Sarwat, and S. Bhansali, "Machine learning techniques in wireless sensor  
358 network based precision agriculture," *J. Electrochem. Soc.* **167**, 037522 (2019).
- 359 18. S. Riurean, T. Antipova, Á. Rocha, M. Leba, and A. Ionica, "Vlc, occ, ir and lifi reliable optical wireless technologies  
360 to be embedded in medical facilities and medical devices," *J. medical systems* **43**, 1–10 (2019).
- 361 19. M. F. Ahmed, M. K. Hasan, M. Z. Chowdhury, N. C. Hoan, and Y. M. Jang, "Continuous status monitoring of  
362 industrial valve using occ-enabled wireless sensor network," *IEEE Transactions on Instrumentation Meas.* (2021).
- 363 20. B. Donmez, R. Mitra, and F. Miramirkhani, "Channel modeling and characterization for vlc-based medical body  
364 sensor networks: Trends and challenges1," *IEEE Access* (2021).
- 365 21. O. Haddad, M.-A. Khalighi, S. Zvanovec, and M. Adel, "Channel characterization and modeling for optical wireless  
366 body-area networks," *IEEE Open J. Commun. Soc.* **1**, 760–776 (2020).
- 367 22. P. Agheli, H. Beyranvand, and M. J. Emadi, "Uav-assisted underwater sensor networks using rf and optical wireless  
368 links," *J. Light. Technol.* **39**, 7070–7082 (2021).
- 369 23. X. Liu, X. Wei, L. Guo, Y. Liu, Q. Song, and A. Jamalipour, "Turning the signal interference into benefits: Towards  
370 indoor self-powered visible light communication for iot devices in industrial radio-hostile environments," *IEEE*  
371 *Access* **7**, 24978–24989 (2019).
- 372 24. T. Kamalakis, Z. Ghassemlooy, S. Zvanovec, and L. N. Alves, "Analysis and simulation of a hybrid visible-light/infrared  
373 optical wireless network for iot applications," *J. Opt. Commun. Netw.* **14**, 69–78 (2022).
- 374 25. G. Ntogari, T. Kamalakis, and T. Sphicopoulos, "Performance analysis of non-directed equalized indoor optical  
375 wireless systems," in *2008 6th International Symposium on Communication Systems, Networks and Digital Signal*  
376 *Processing*, (IEEE, 2008), pp. 156–160.
- 377 26. J. R. Barry, J. M. Kahn, W. J. Krause, E. A. Lee, and D. G. Messerschmitt, "Simulation of multipath impulse response  
378 for indoor wireless optical channels," *IEEE journal on selected areas communications* **11**, 367–379 (1993).
- 379 27. T. Kamalakis, L. Dogkas, and F. Simou, "Optimization of a discrete multi-tone visible light communication system  
380 using a mixed-integer genetic algorithm," *Opt. Commun.* **485**, 126741 (2021).
- 381 28. T. Kamalakis, "Pyowiot," <https://github.com/thomaskamalakis/pyowiot> (2022).
- 382 29. J. Lopez-Hernandez, R. Perez-Jimenez, and A. Santamaria, "Modified monte carlo scheme for high-efficiency  
383 simulation of the impulse response on diffuse ir wireless indoor channels," *Electron. Lett.* **34**, 1819–1820 (1998).
- 384 30. M. B. Rahaim, J. Morrison, and T. D. Little, "Beam control for indoor fso and dynamic dual-use vlc lighting systems,"  
385 *J. Commun. Inf. Networks* **2**, 11–27 (2017).